Electronic Supplementary Information

Nb-doped layered FeNi phosphide nanosheets for highly-efficient overall water splitting under high current densities

Shuting Wen,[a] Guangliang Chen,*[a] Wei Chen,*[b] Mengchao Li,[b] Bo Ouyang,*[c] Xingquan Wang,[b] Dongliang Chen,[a] Teng Gong,[b] Xianhui Zhang,[d] Jun Huang*[b,e] and Kostya (Ken) Ostrikov[e,f]

[a]School of Materials Science and Engineering, Zhejiang Sci-Tech University, Hangzhou 310018, People's Republic of China

*E-mail: glchen@zstu.edu.cn

[b]School of Physics and Electronic Information, Gannan Normal University, Ganzhou, Jiangxi 341000, People's Republic of China

*E-mail: chwbetter@163.com; junhuang66@163.com

[c]Department of Applied Physics & Institution of Energy & Microstructure, Nanjing University of Science & Technology, Nanjing 210094, People's Republic of China

*E-mail: ouyangboyi@outlook.com

[d]Institute of Electromagnetics and Acoustics, Fujian Provincial Key Laboratory of Plasma and Magnetic Resonance, Department of Electronic Science, Xiamen University, Xiamen 361005, People's Republic of China

[e]School of Chemistry and Physics, Queensland University of Technology, Brisbane, QLD 4000, Australia

[f]Centre for Materials Science, Queensland University of Technology, Brisbane, QLD 4000, Australia

1. Experimental

1.1 Fabrication of NiFe LDH-Nb_2O_5/PNF

For getting a clear reactive substrate, the NF (1 × 3 cm) was respectively washed with acetone and 10 wt % hydrochloric acid solution for 10 minutes in an ultrasonic device, and the sample was rinsed three times with absolute ethanol and deionized water, respectively. Then, the washed NF was contained in an air-oven at 50 °C for 4 hours and weigh the sample mass. Subsequently, both sides of the NF substrate were treated by the DBD plasma for about 15 min (PNF). The NiFe LDH-Nb_2O_5/PNF was successfully fabricated with a facile hydrothermal method. In brief, 1.5 mmol $Ni(NO_3)_2·6H_2O$, 0.167 mmol $Fe(NO_3)_3·9H_2O$, 0.333 mmol $NbCl_5$, 5 mmol urea and 2.5 mmol NH_4F were dissolved into 20 ml deionized water and stirred by a magnetic device until a uniform solution was formed. The prepared solution and PNF (1 × 3 cm) were added into a 30 mL reactive autoclave and kept at 150 °C for 10 hours. After the reaction, the autoclave was cooled down to 20 °C and the fabricated samples were repeatedly cleared with 99.9 % ethanol and deionized water for 3 times. Finally, the samples were dried for 6 hours at 50 °C for subsequent reactions. In addition, the catalysts fabricated with different reaction parameters were also explored for the comparison purposes.

1.2 Fabrication of $Ni_{12}P_5$-Fe_2P-NbP/PNF structures

The prepared NiFe LDH-Nb_2O_5/PNF (1 × 1 cm) and 0.2 g red phosphorus powder were put into the corundum boats. The red phosphorus powder was placed in the upstream position, and the NiFe LDH-Nb_2O_5/PNF was placed in the downstream location of the tube reactor. Then, the tubular furnace was heated to 500 °C at a heating rate of 5 °C min^{-1} and maintained for 2 h under a nitrogen ambient condition. As a result, the NiFeNb phosphide was obtained after it was cooled to room temperature, and the catalyst mass formed on the PNF surface was also detected (2.5 mg cm^{-2}).

1.3 Structure characterization

The surface structure of $Ni_{12}P_5$-Fe_2P-NbP nano-flakes on PNF was detected by using the field-emission scanning electron microscope or transmission electron microscope, as well as their EDS mapping images. The evolution of the crystal phases and the elemental states of $Ni_{12}P_5$-Fe_2P-NbP before and after HER and ORE processes were analyzed by using X-ray diffractometer (XRD) and X-ray photoelectron spectroscopy (XPS), respectively. The frame structure of $Ni_{12}P_5$-Fe_2P-NbP/PNF after a prolonged electrolysis was detected by a Raman spectrometer. Noted that all the measuring systems and testing conditions are similar with those used in our previous work.[S1]

1.4 Electrochemical evaluation

The electrochemical properties of the resulting catalysts were tested in a standard three-electrode cell in 1 M KOH solution (pH 14) by using an electrochemical workstation (Model: CHI 660E, Shanghai Chenhua Instrument Co, Ltd) at 25 ℃. The testing cell contained a working electrode of electrocatalyst, a reference electrode of Hg/Hg_2Cl_2 (saturated KCl solution) and a counter electrode of carbon rod. All obtained potentials were calibrated to a reversible hydrogen electrode (RHE) using the calculation method given in reference.[S2] In brief, the catalyst was cut into 0.5 × 0.5 cm (0.25 cm^{-2}), and activated by a cyclic voltammetry (CV) scanning for 800 cycles to ensure the stability and accuracy of detected results. Then, the measurements of linear sweep voltammetry (LSV), *iR*-compensating LSV, electrochemical impedance spectroscopy (EIS), the electrochemical active surface area (ECSA), and turnover frequency (TOF) values were performed with similar methods reported in the previous works.[S3-S5] For comparison, the electrocatalytic performances of PNF coated with 20 wt % Pt/C for HER electrode and RuO_2 for OER electrode, which has the same loading rate as $Ni_{12}P_5$-Fe_2P-NbP (2.5

mg cm^{-2}), were also studied. In addition, the electrocatalytic durability and stability of the as-prepared catalysts were indicated by the measured chronoamperometric curves (*I-t*) at j_{100} and j_{300} for 100 h. Furthermore, a simple drainage method was used to detect the generation efficiency of hydrogen and oxygen, and the volume of exhaust gas was recorded each 10 minutes. Finally, a two-electrode cell equipped with $Ni_{12}P_5$-Fe_2P-NbP/PNF electrodes was assembled to explore the bifunctional performance of the catalyst for overall water splitting, as well as to measure the long-term *I-t* curve under the constant current density of j_{10}.

1.5 Theory simulations

Herein, the density functional theory (DFT) calculations are performed following the similar methods explained previously.[S4] Briefly, the interaction between the ions and electrons is described according to the projector augmented wave (PAW) method. The vacuum layer is set to 20 Å along the perpendicular direction of the atomistic models to inhibit the interaction between periodical cells. The kinetic cutoff energy was set to 500 eV along with the *k*-point mesh of 2×2×1 for all the cells. In terms of the structural optimization, atomic positions, shape and volume of all the cells can relax in all directions until the total energy and forces are converged within less than 10^{-5} eV per atom and 0.01 eV $Å^{-1}$, respectively.

According to HER dynamics, the hydrogen intermediate was adsorbed onto surfaces of $Ni_{12}P_5$, Fe_2P and NbP, denoted as H*. The reaction could be expressed as:

$* + H^+ \rightarrow H^* + e^-$

$H^* + H^* \rightarrow H_2$

In terms of OER dynamics, the intermediates of O, OH and OOH ions were absorbed on to substrate surfaces, termed as O*, OH* and OOH*. The reaction could be expressed as:

$* + OH^- + e^- \rightarrow OH^*$

$OH^* + OH^- + e^- \rightarrow O^* + H_2O$

$O^* + OH^- + e^- \rightarrow OOH^*$

$OOH^* + OH^- + e^- \rightarrow O_2 + H_2O$

where * stands for an active site on the catalyst surface. OH*, O*, OOH* and H* represent different adsorbed intermediates. Since the Gibbs free energy (△G) can be obtained under the set of standard conditions (T = 298.15 K, pH = 14, external potential = 0), and it can be calculated as follows:

$$\Delta G = \Delta E + \Delta ZPE - \Delta TS ,$$

where △E serves as the absorbed energy between the reactant and product in the reaction. Furthermore, △ZPE and △TS denote the difference of zero-point energy and entropic contribution, respectively.

2. Supplementary Figures

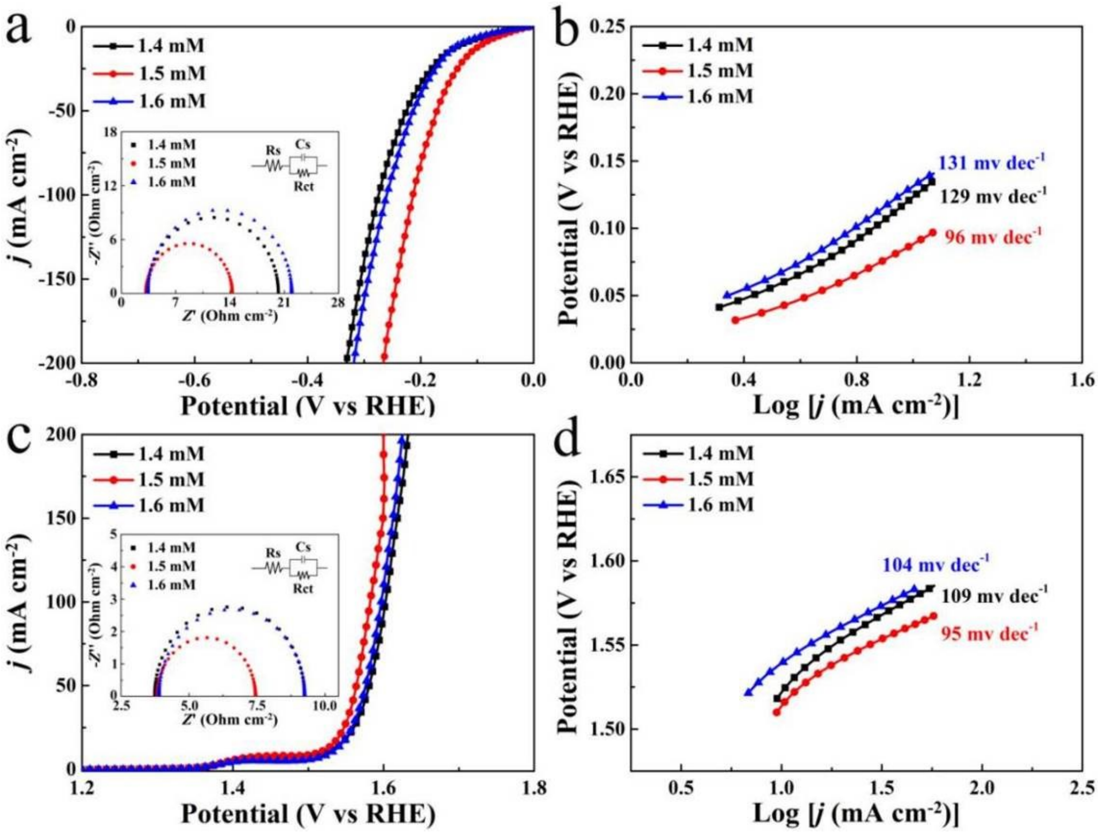

Figure S1. The effects of $Ni(NO_3)_2$ concentration on the HER and OER performances of NiFe LDH-Nb_2O_5/PNF. (a) Polarization curves in 1 M KOH for HER and the insert is the corresponding Nyquist plots, (b) The Tafel plots derived from the data in (a), (c) Polarization curves in 1 M KOH for OER and the insert is the corresponding Nyquist plots, and (d) The Tafel plots derived from the data in (c).

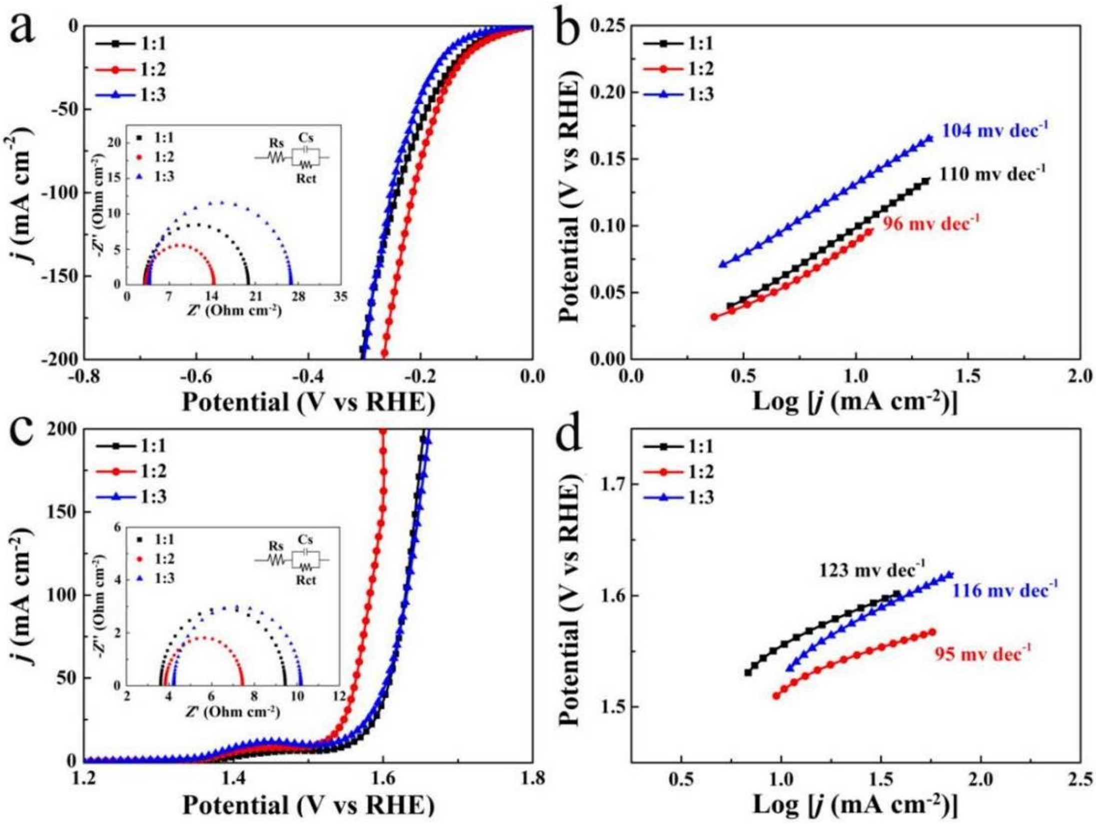

Figure S2. The effects of Fe/Nb ratios on the HER and OER performances of NiFe LDH-Nb_2O_5/PNF. (a) Polarization curves in 1 M KOH for HER and the insert is the corresponding Nyquist plots, (b) The Tafel plots derived from the data in (a), (c) Polarization curves in 1 M KOH for OER and the insert is the corresponding Nyquist plots, and (d) The Tafel plots derived from the data in (c).

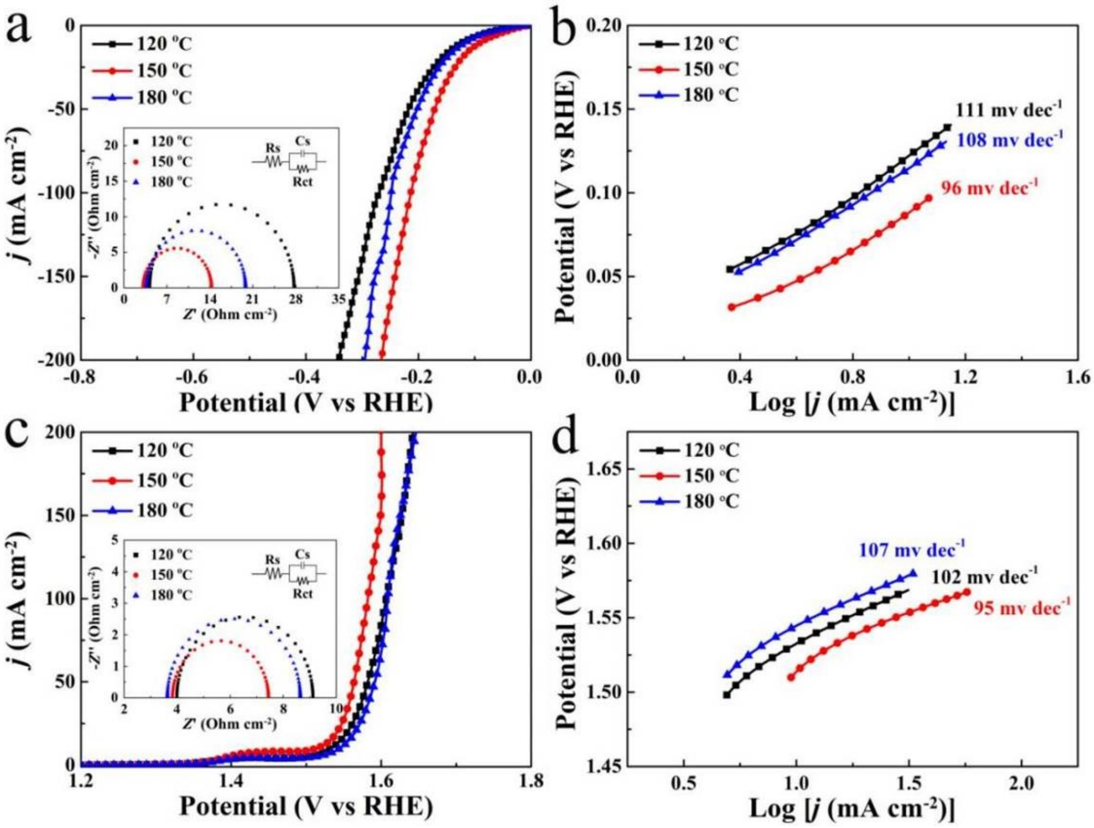

Figure S3. The effects of hydrothermal temperature on the HER and OER performances of NiFe LDH-Nb_2O_5/PNF. (a) Polarization curves in 1 M KOH for HER and the insert is the corresponding Nyquist plots, (b) The Tafel plots derived from the data in (a), (c) Polarization curves in 1 M KOH for OER and the insert is the corresponding Nyquist plots, and (d) The Tafel plots derived from the data in (c).

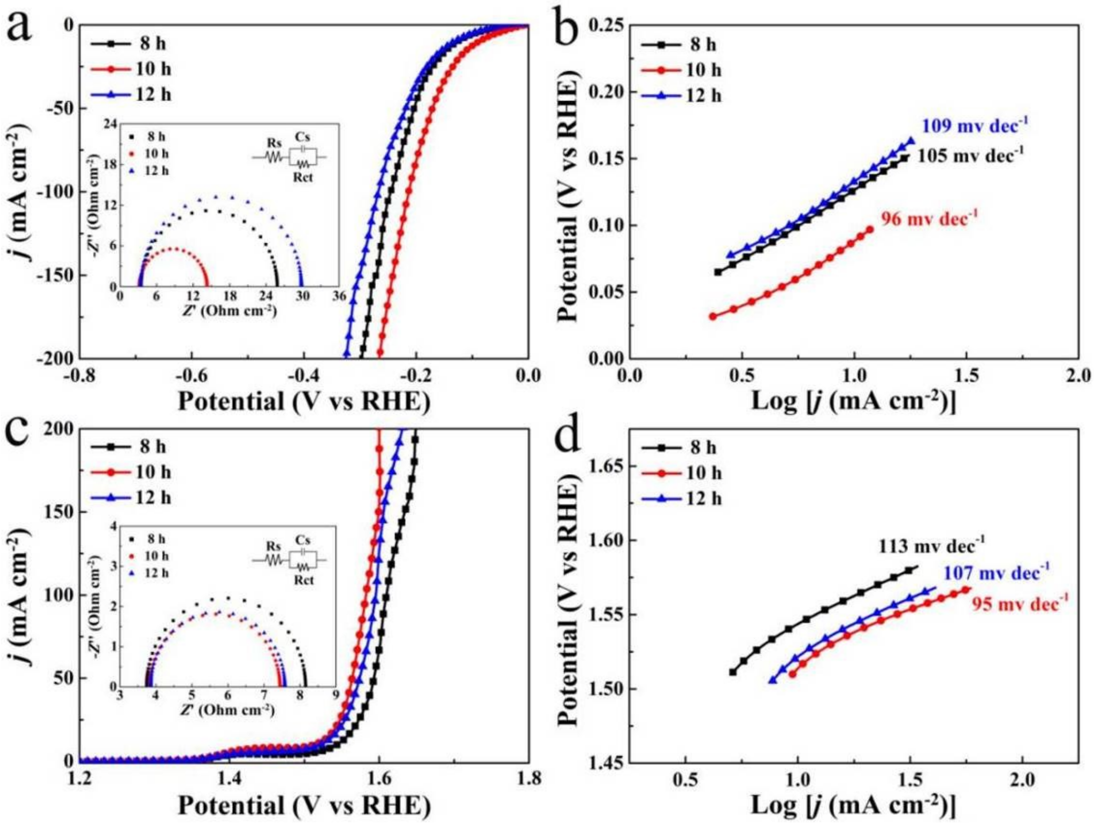

Figure S4. The effects of hydrothermal reaction time on the HER and OER performances of NiFe LDH-Nb_2O_5/PNF. (a) Polarization curves in 1 M KOH for HER and the insert is the corresponding Nyquist plots, (b) The Tafel plots derived from the data in (a), (c) Polarization curves in 1 M KOH for OER and the insert is the corresponding Nyquist plots, and (d) The Tafel plots derived from the data in (c).

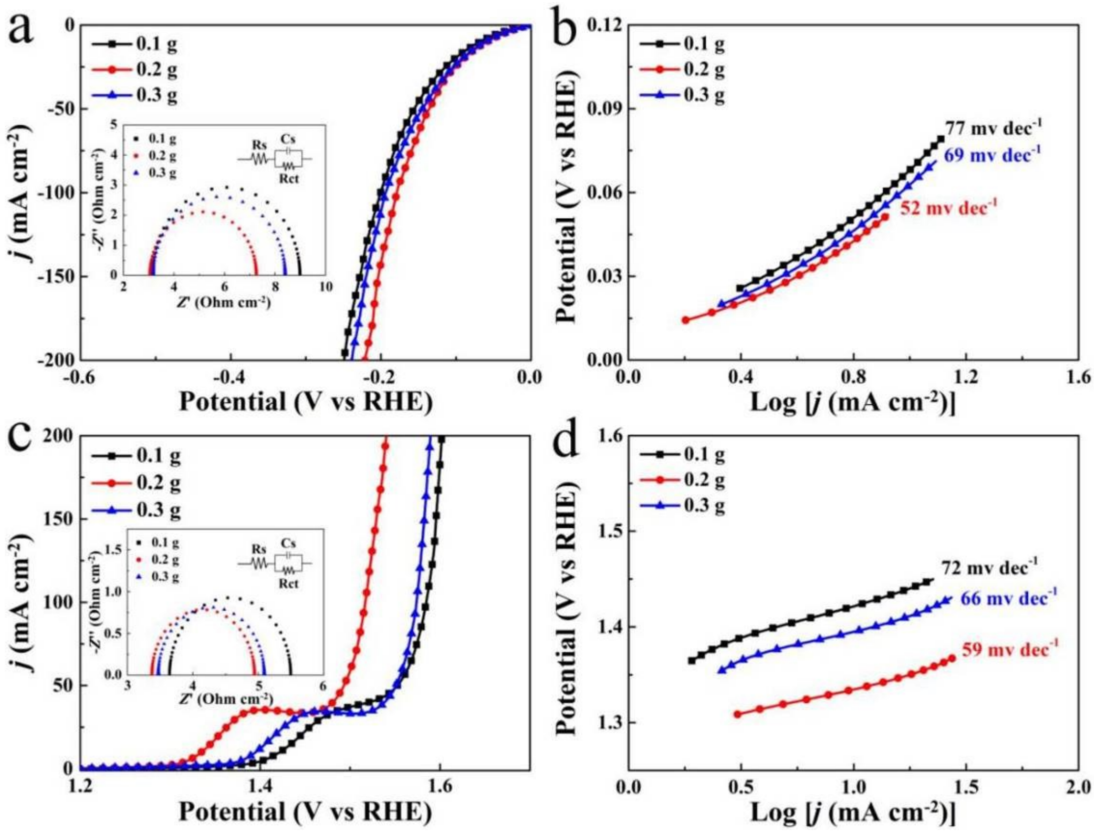

Figure S5. The effects of red phosphorus amounts on the HER and OER performances of $Ni_{12}P_5$-Fe_2P-NbP/PNF. (a) Polarization curves in 1 M KOH for HER and the insert is the corresponding Nyquist plots, (b) The Tafel plots derived from the data in (a), and (c) Polarization curves in 1 M KOH for OER and the insert is the corresponding Nyquist plots, and (d) The Tafel plots derived from the data in (c).

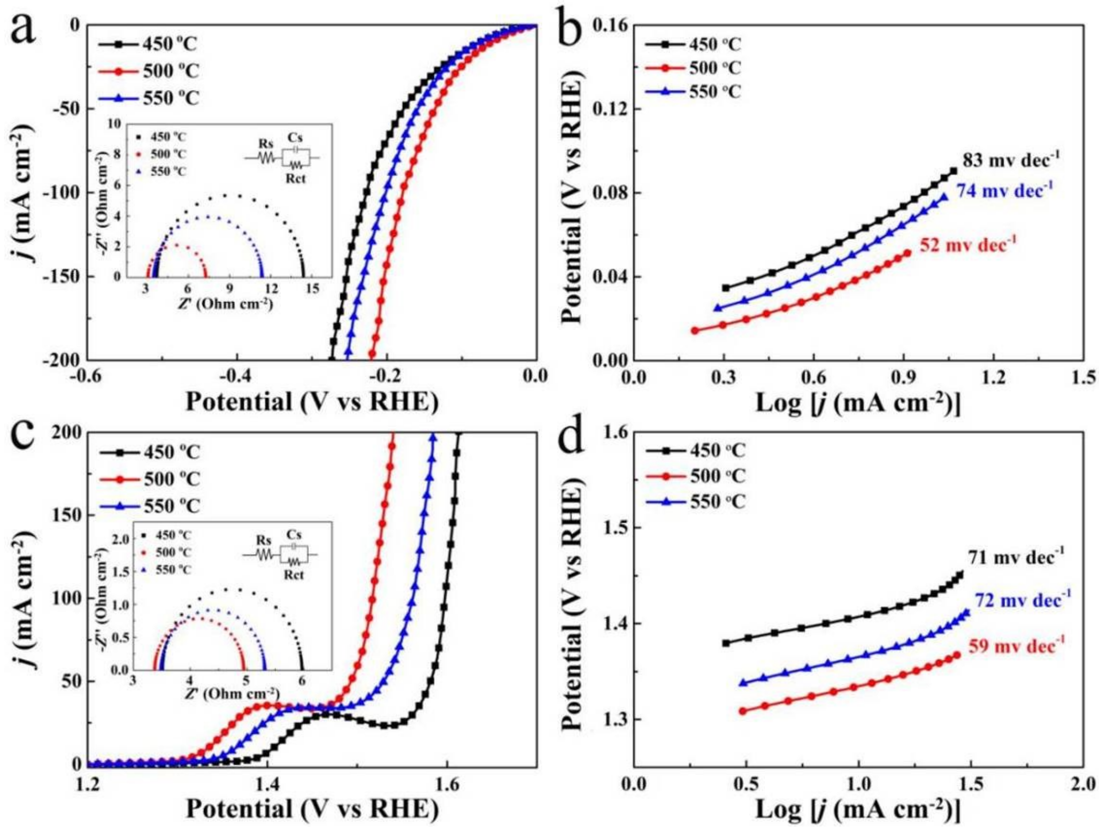

Figure S6. The effects of phosphating reaction temperature on the HER and OER performances of $Ni_{12}P_5$-Fe_2P-NbP/PNF. (a) Polarization curves in 1 M KOH for HER and the insert is the corresponding Nyquist plots, (b) The Tafel plots derived from the data in (a), (c) Polarization curves in 1 M KOH for OER and the insert is the corresponding Nyquist plots, and (d) The Tafel plots derived from the data in (c).

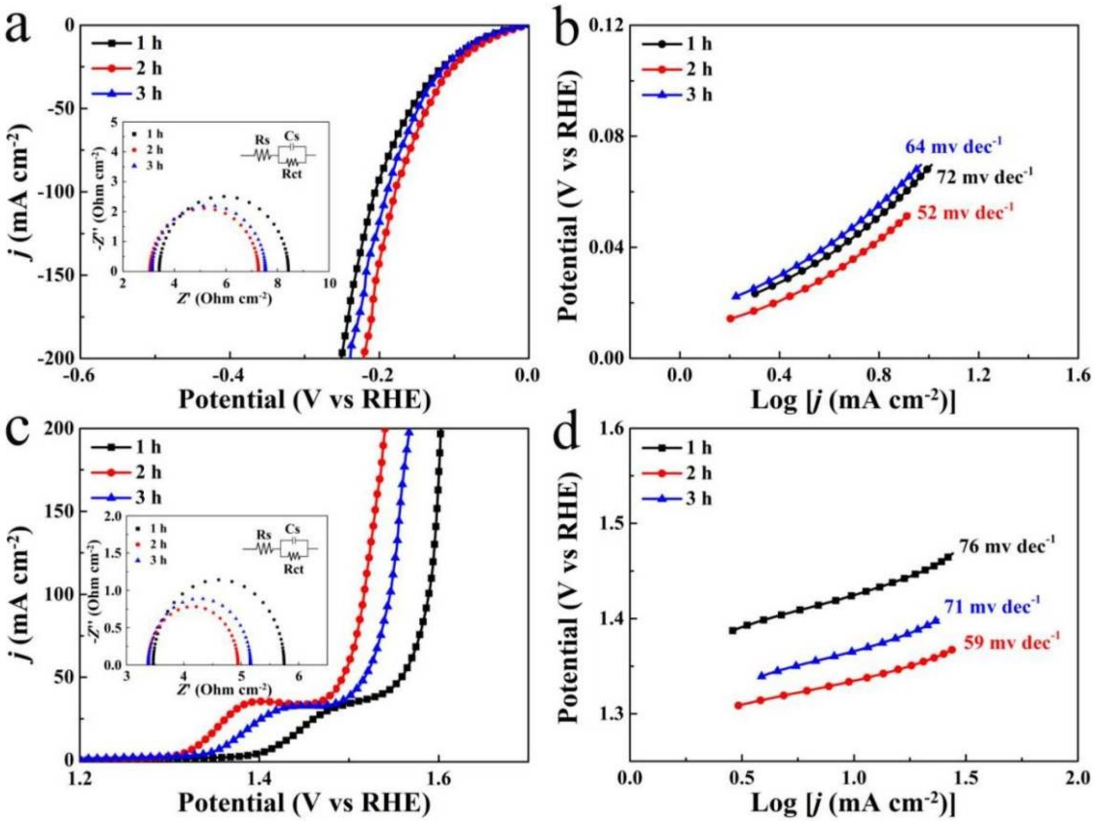

Figure S7. The effects of phosphating reaction time on the HER and OER performances of $Ni_{12}P_5$-Fe_2P-NbP/PNF. (a) Polarization curves in 1 M KOH for HER and the insert is the corresponding Nyquist plots, (b) The Tafel plots derived from the data in (a), (c) Polarization curves in 1 M KOH for OER and the insert is the corresponding Nyquist plots, and (d) The Tafel plots derived from the data in (c).

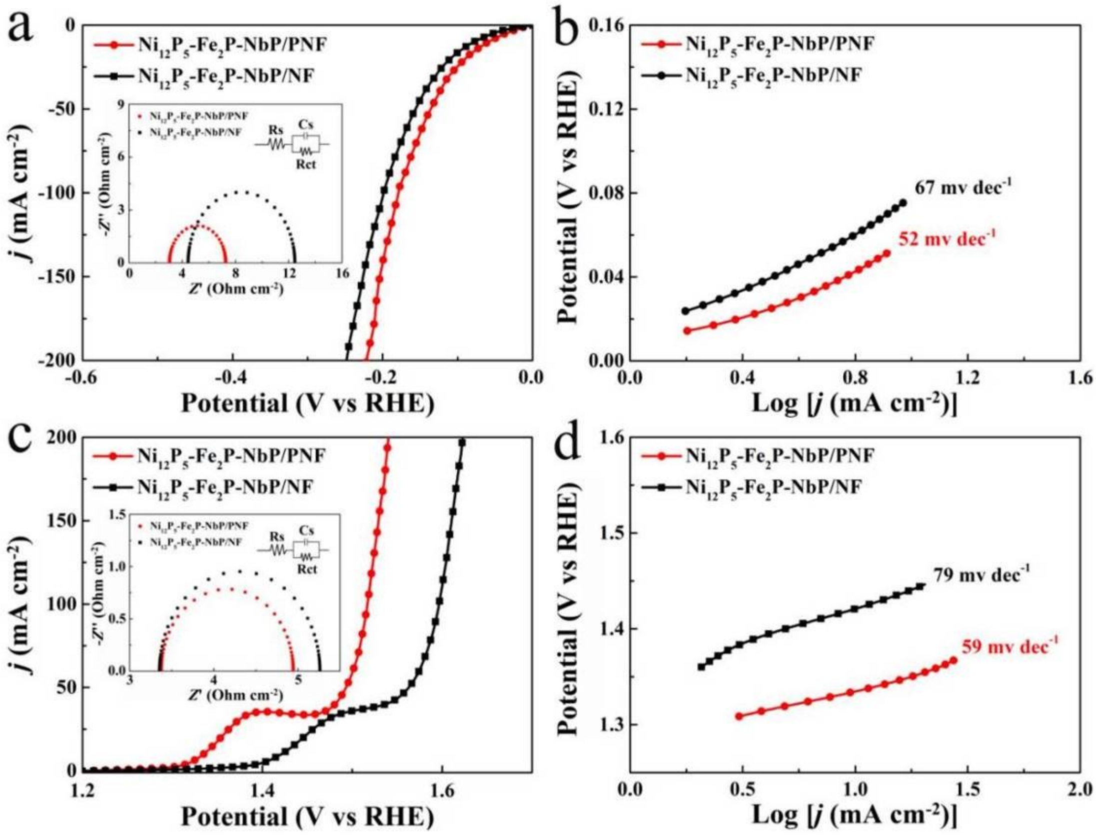

Figure S8. The effects of DBD treatment on the HER and OER of $Ni_{12}P_5$-Fe_2P-NbP electrocatalysts. (a) Polarization curves in 1 M KOH for HER and the insert is the corresponding Nyquist plots, (b) The Tafel plots derived from the data in (a), (c) Polarization curves in 1 M KOH for OER and the insert is the corresponding Nyquist plots, and (d) The Tafel plots derived from the data in (c).

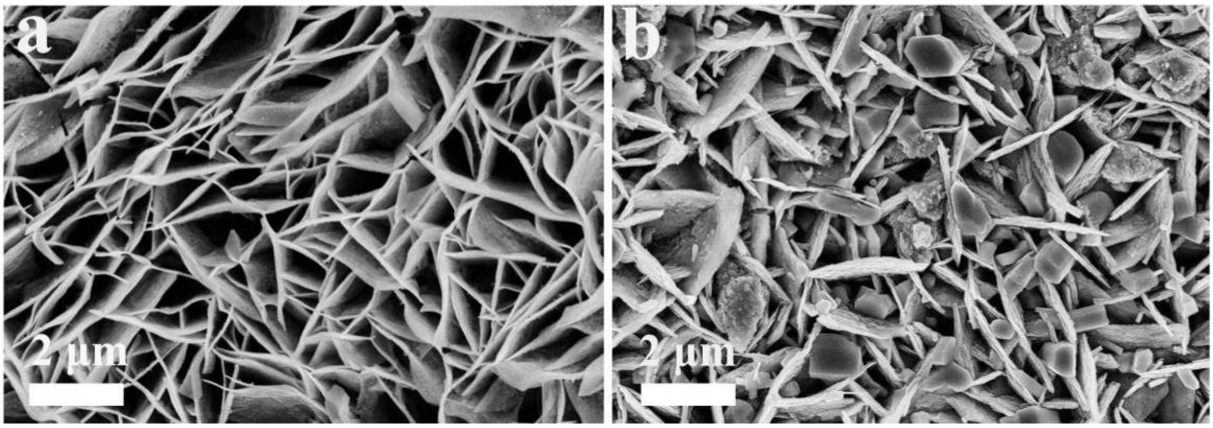

Figure S9. SEM images of $NiFeP_x$/PNF (a) and $NiNbP_x$/PNF (b).

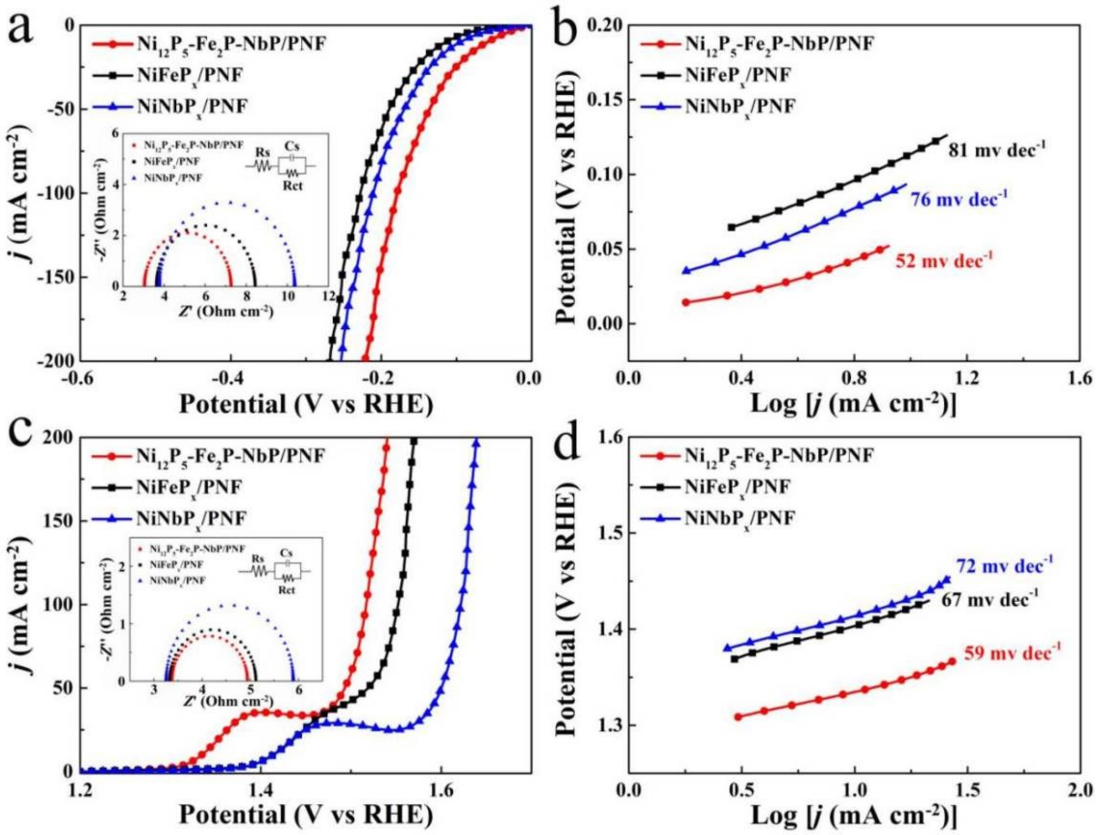

Figure S10. The HER and OER performances for $Ni_{12}P_5$-Fe_2P-NbP/PNF, $NiFeP_x$/PNF, and $NiNbP_x$/PNF. (a) Polarization curves in 1 M KOH for HER and the insert is the corresponding Nyquist plots, (b) The Tafel plots derived from the data in (a), (c) Polarization curves in 1 M KOH for OER and the insert is the corresponding Nyquist plots, and (d) The Tafel plots derived from the data in (c).

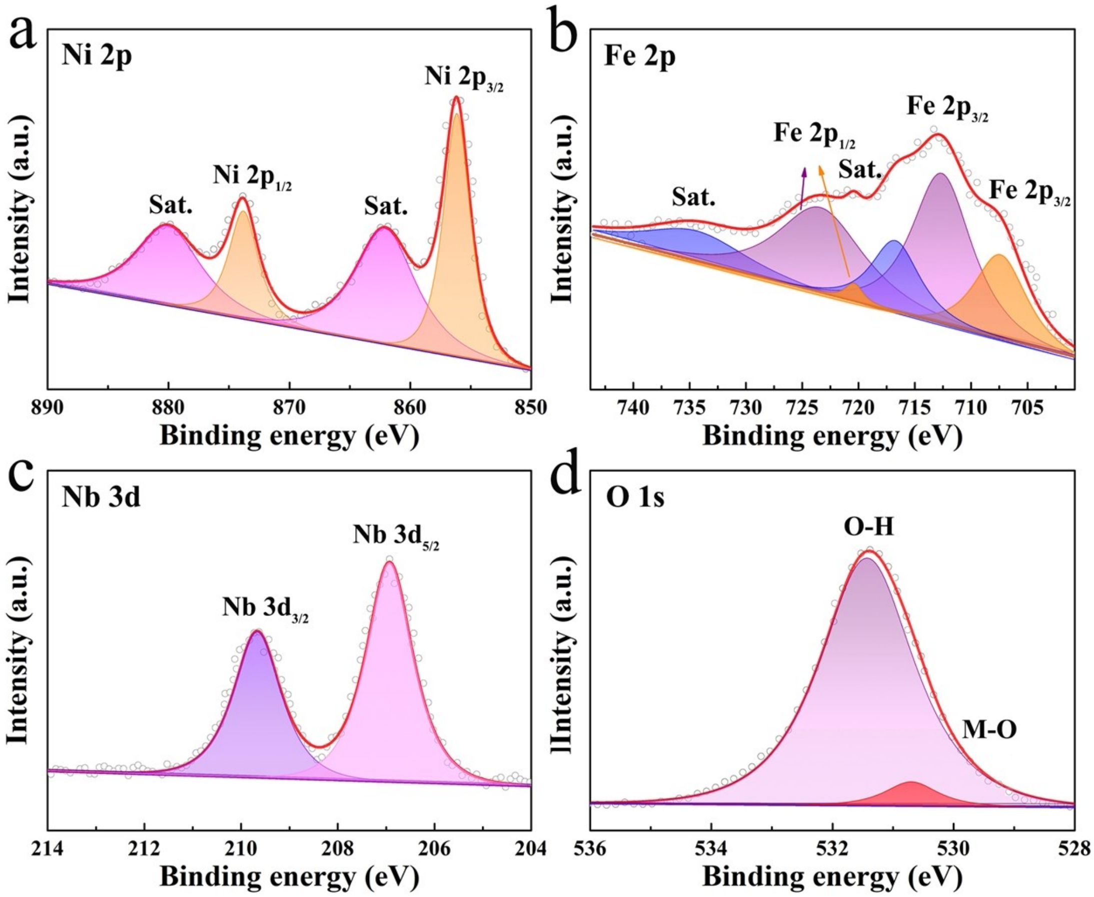

Figure S11. The high resolution XPS spectra of NiFe LDH-Nb_2O_5/PNF. (a) Ni 2p, (b) Fe 2p, (c) Nb 3d, and (d) O 1s.

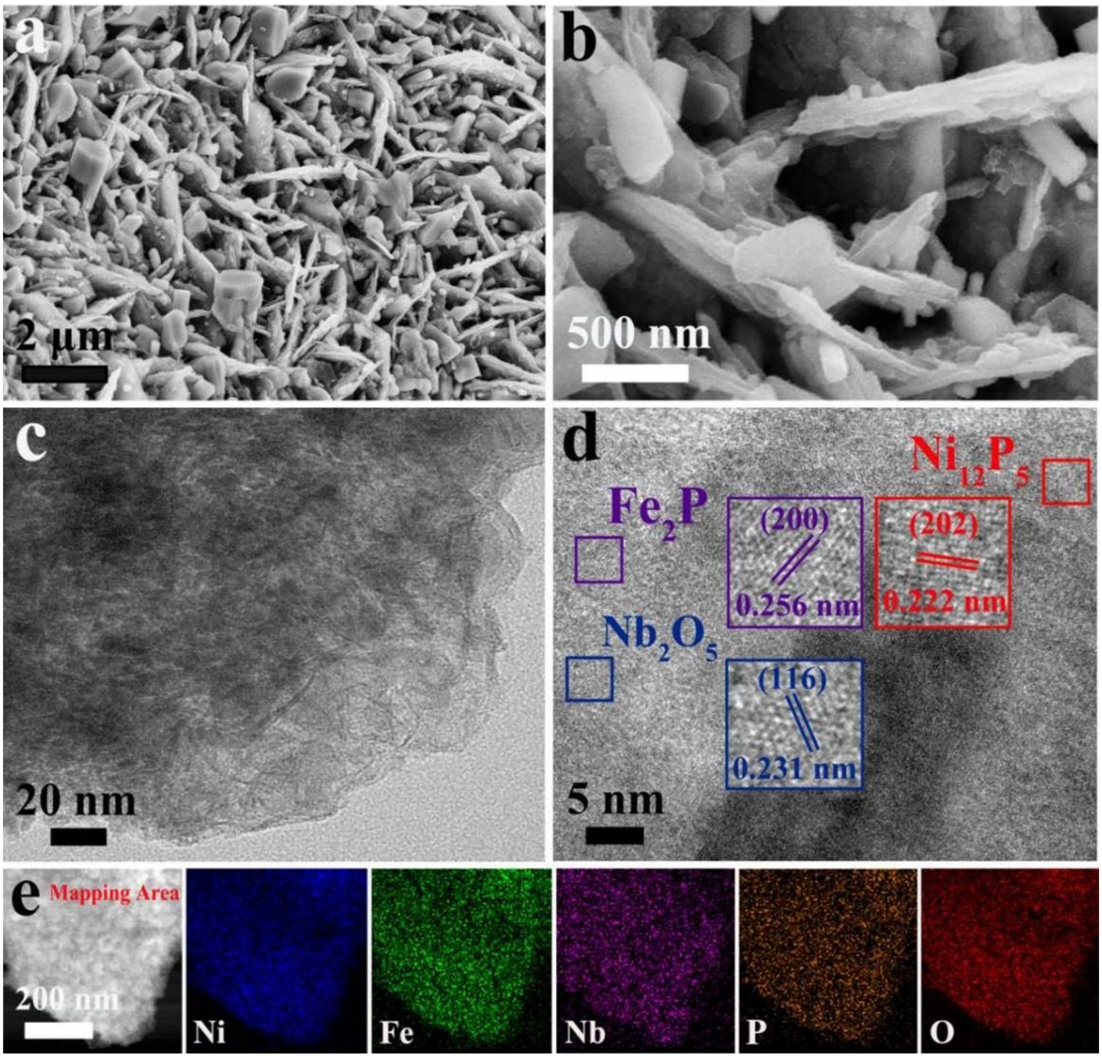

Figure S12. The morphology and crystal structures of $Ni_{12}P_5$-Fe_2P-NbP/PNF after 100 h HER processes at a current density of j_{300} in 1 M KOH solution. (a) Low and (b) High resolution SEM images, (c) Low and (d) High magnification TEM images, and (e) The elements mapping of Ni, Fe, Nb, P and O distributed on the nanosheet.

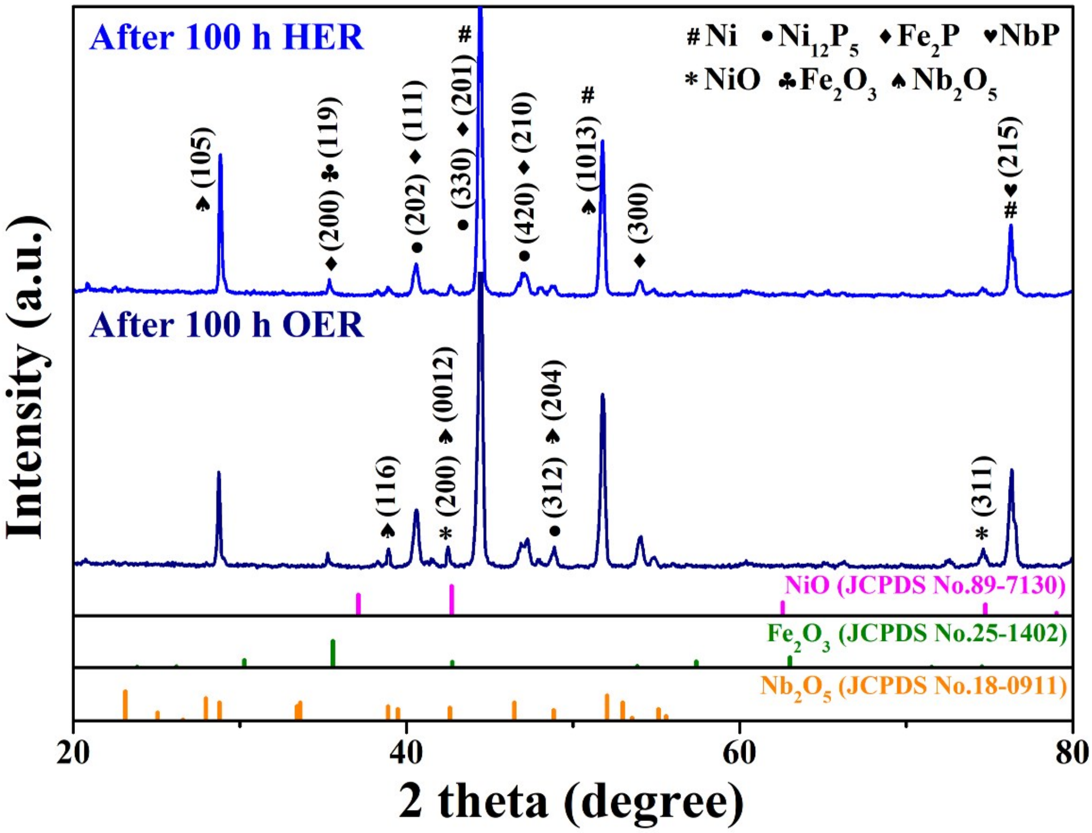

Figure S13. The XRD patterns of the $Ni_{12}P_5$-Fe_2P-NbP/PNF after 100 h HER and OER processes at a current density of j_{300} in 1 M KOH.

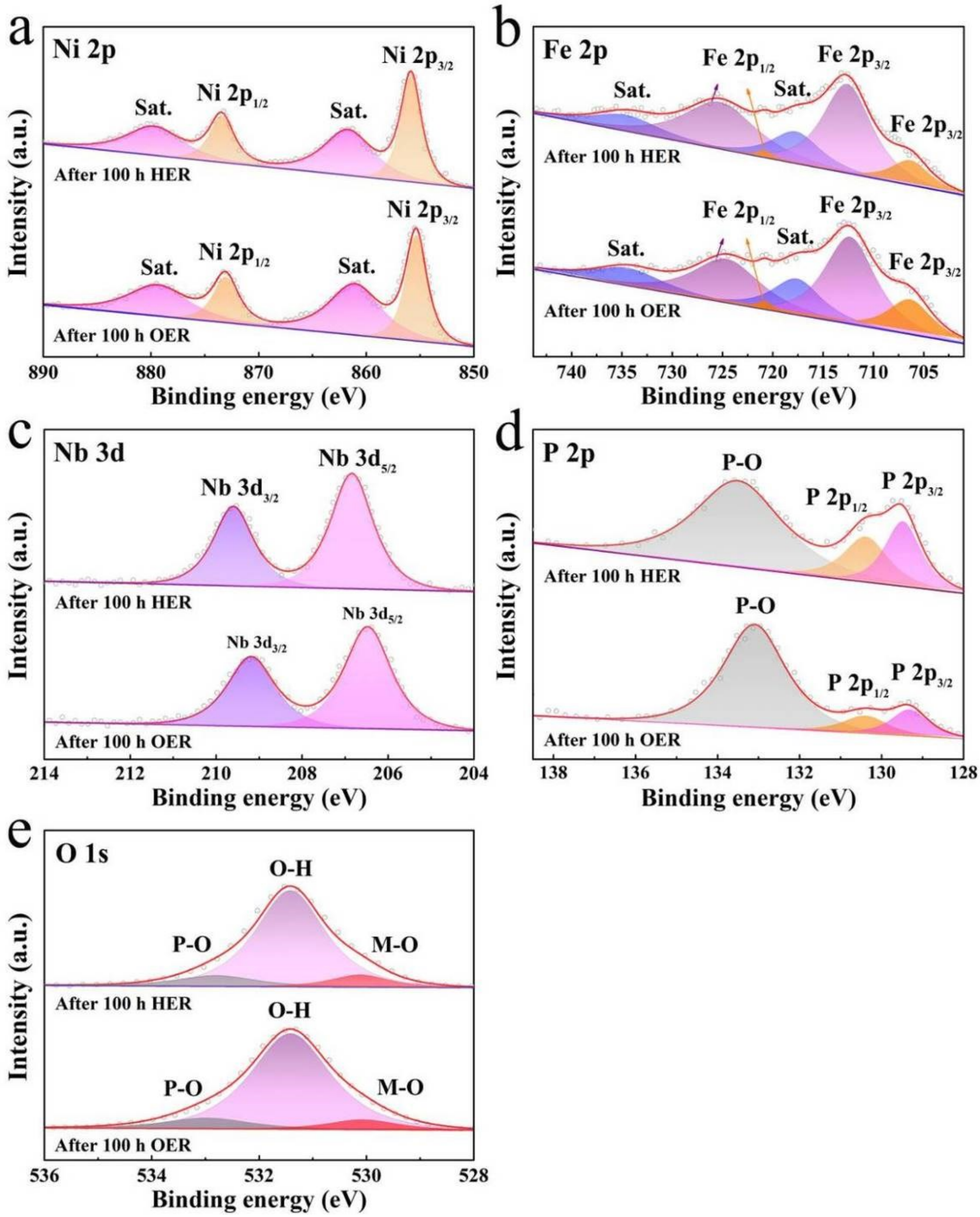

Figure S14. High resolution XPS spectra of $Ni_{12}P_5$-Fe_2P-NbP/PNF after 100 h HER and OER tests at a current density of j_{300} in 1 M KOH. (a) Ni 2p, (b) Fe 2p, (c) Nb 3d, (d) P 2p, and (e) O 1s.

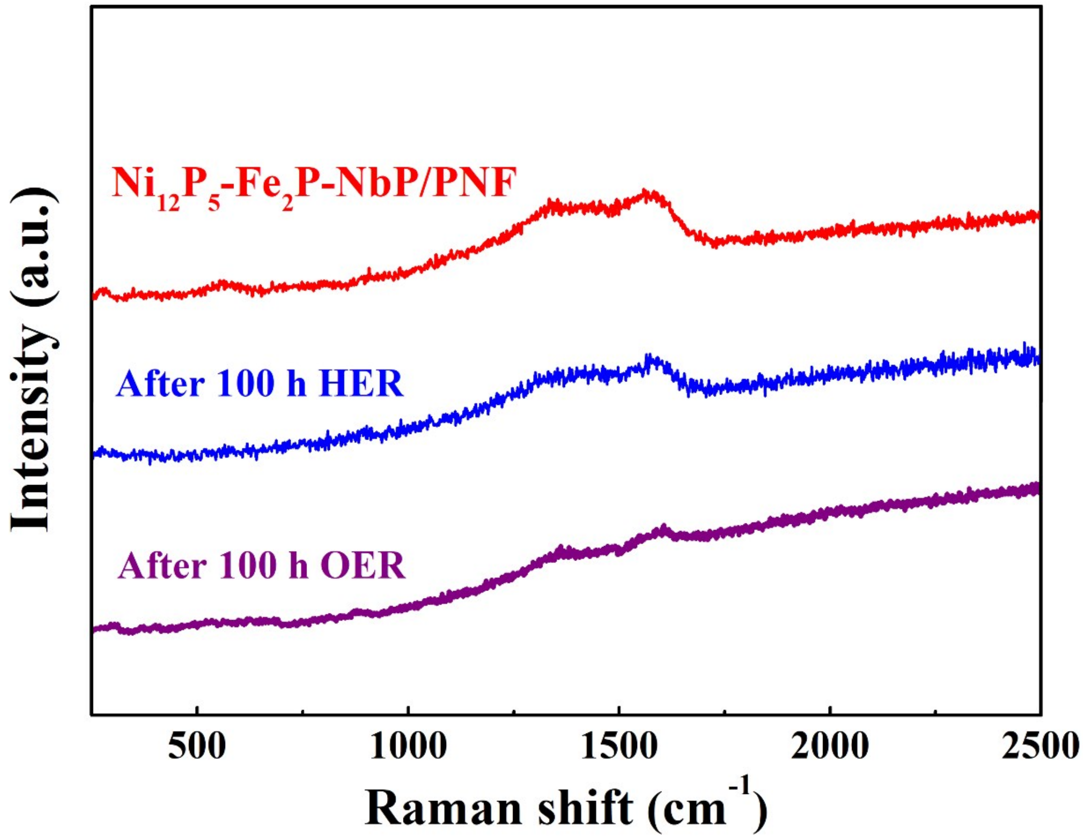

Figure S15. Raman spectra of $Ni_{12}P_5$-Fe_2P-NbP/PNF undergoing long-term HER and OER processes.

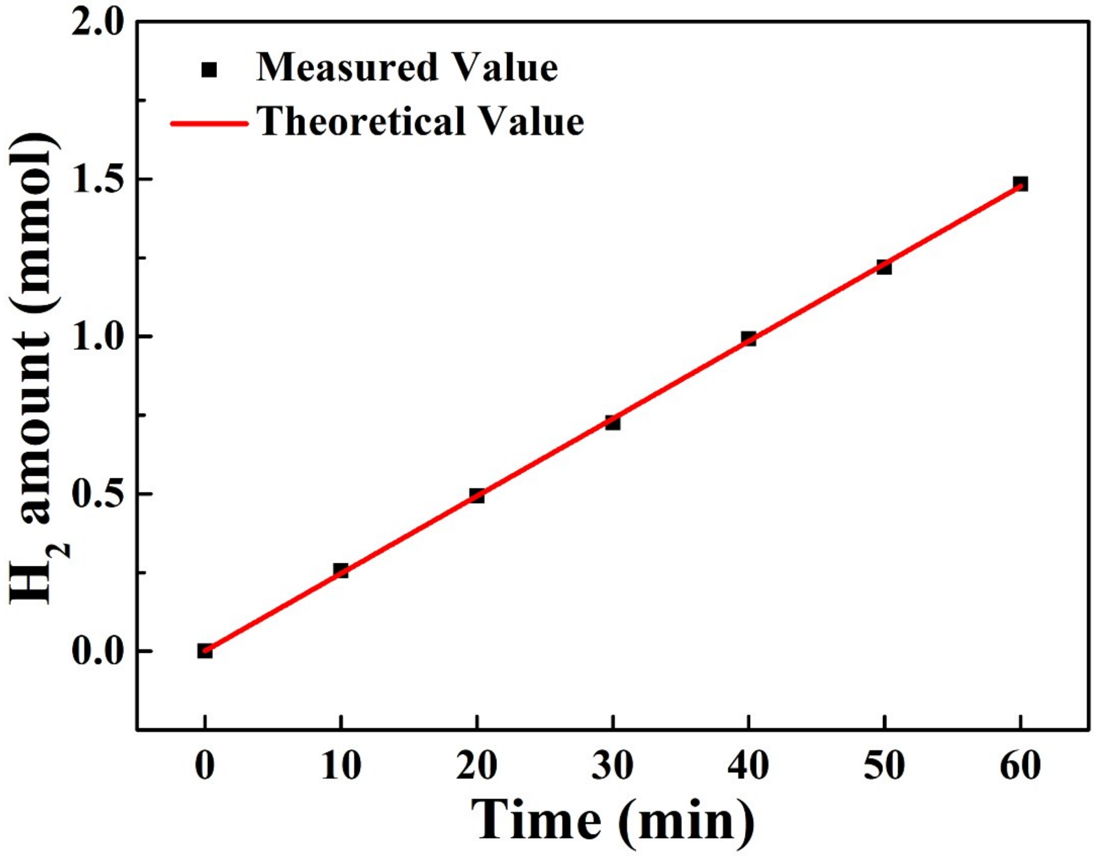

Figure S16. The H_2 amount of $Ni_{12}P_5$-Fe_2P-NbP/PNF generated at a current density of 10 mA cm^{-2}.

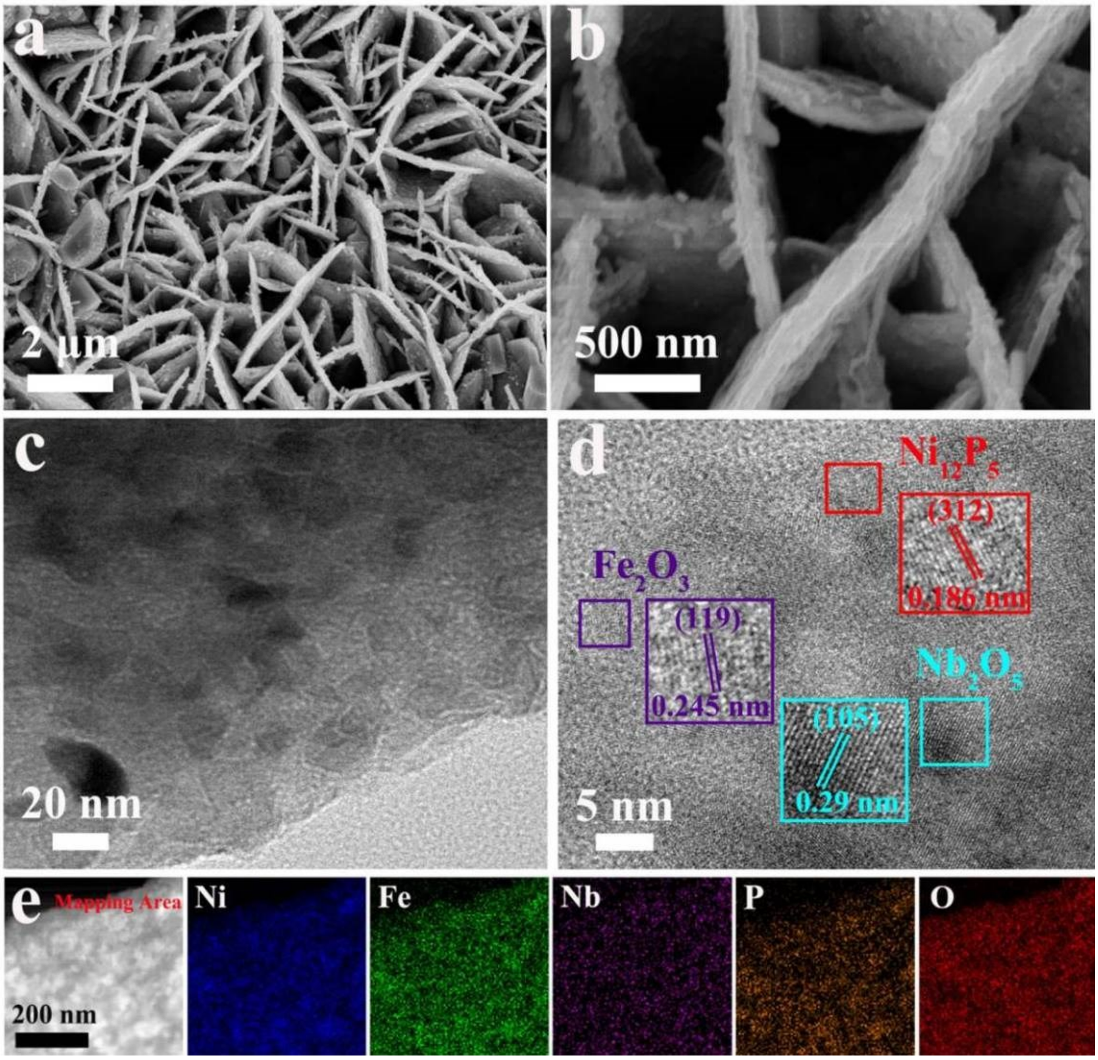

Figure S17. The morphology and crystal structures of $Ni_{12}P_5$-Fe_2P-NbP/PNF after 100 h OER processes at a current density of j_{300} in 1 M KOH. (a) Low and (b) high resolution SEM images, (c) Low and (d) high magnification TEM images, and (e) The elements mapping of Ni, Fe, Nb, P and O distributed on the nanosheet.

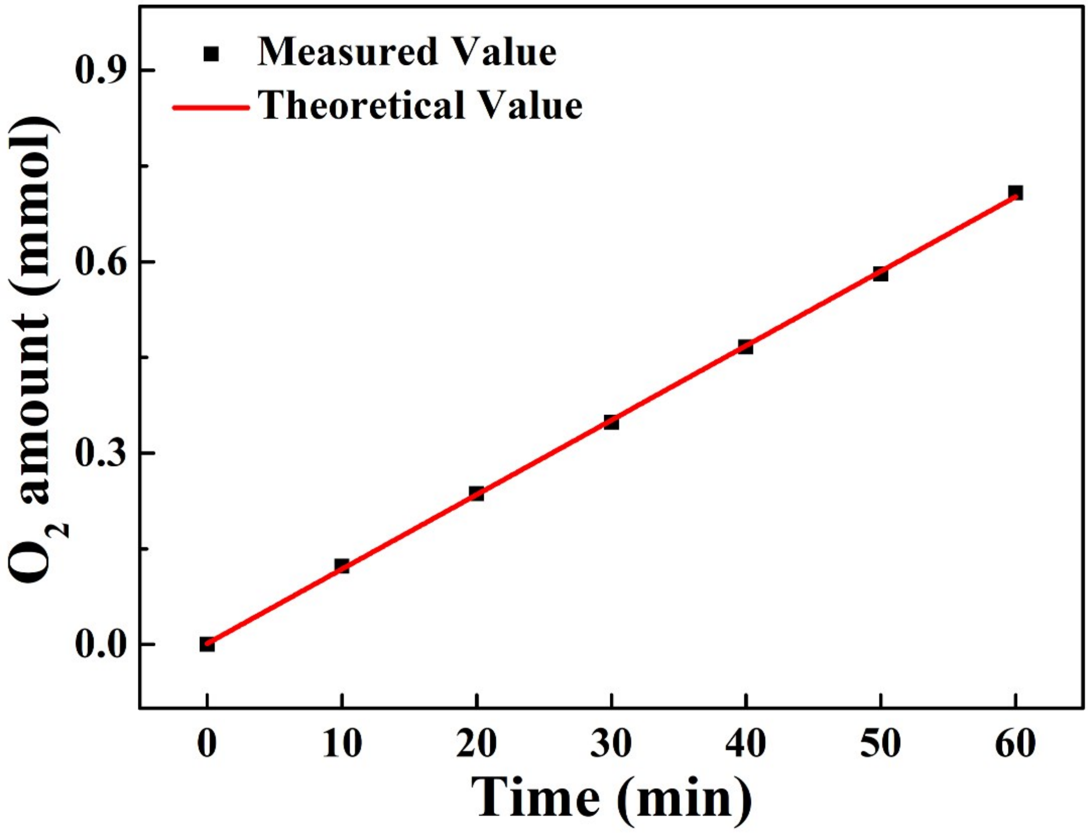

Figure S18. The O_2 amount of $Ni_{12}P_5$-Fe_2P-NbP/PNF generated at a current density of 10 mA cm^{-2}.

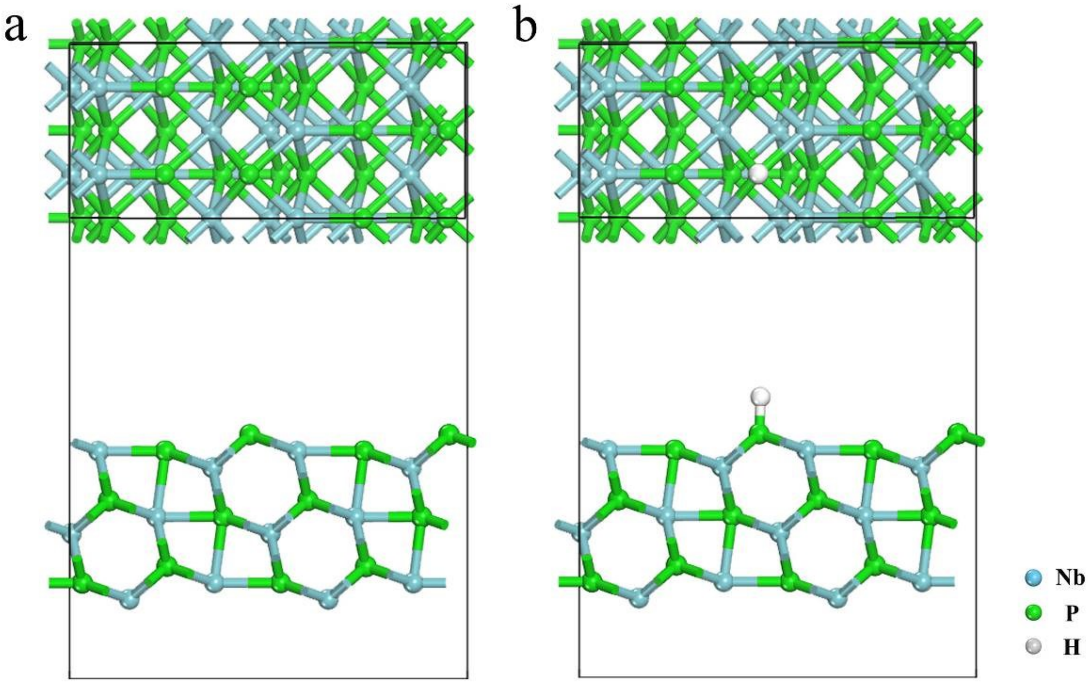

Figure S19. Adsorption of H on the (103) surface of NbP, involved in the HER process.

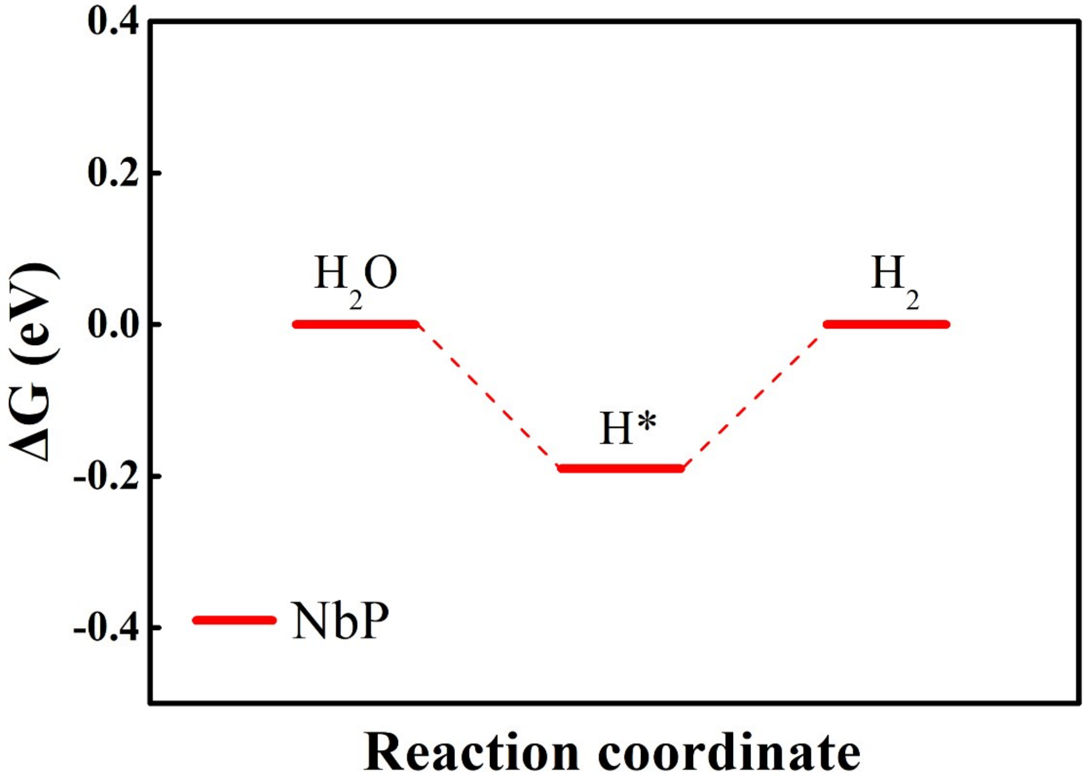

Figure S20. Gibbs free energy of NbP in the HER process.

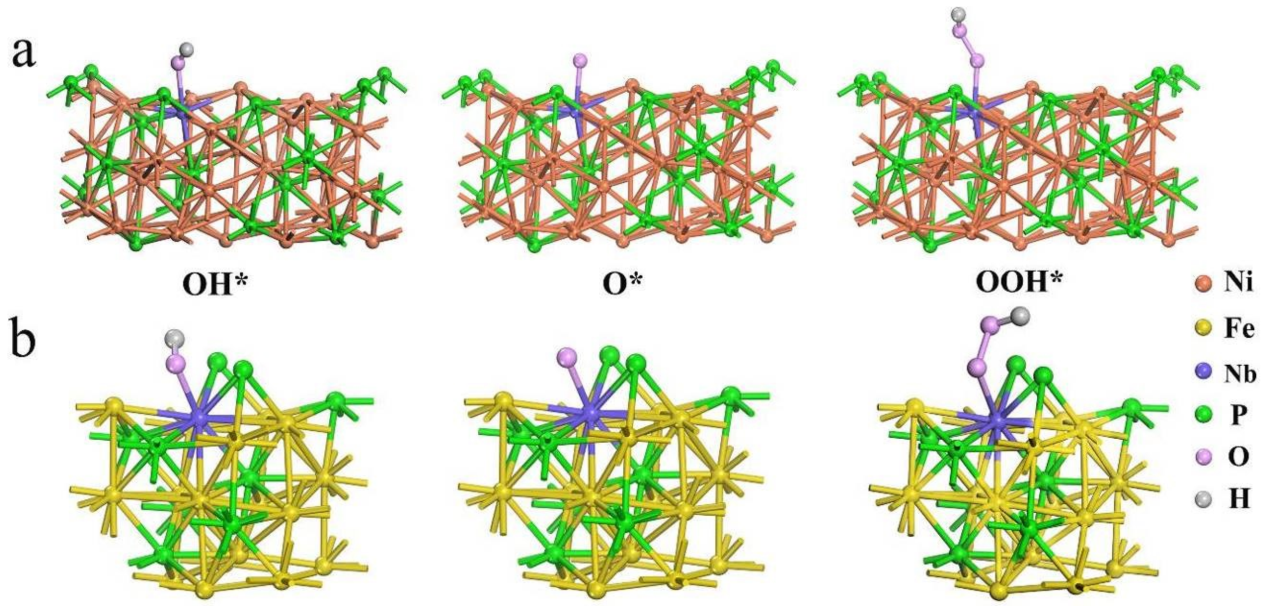

Figure S21. Adsorption geometries of the intermediates OH*, O* and OOH* on the Nb-$Ni_{12}P_5$ (a) and Nb-Fe_2P (b) in the OER process.

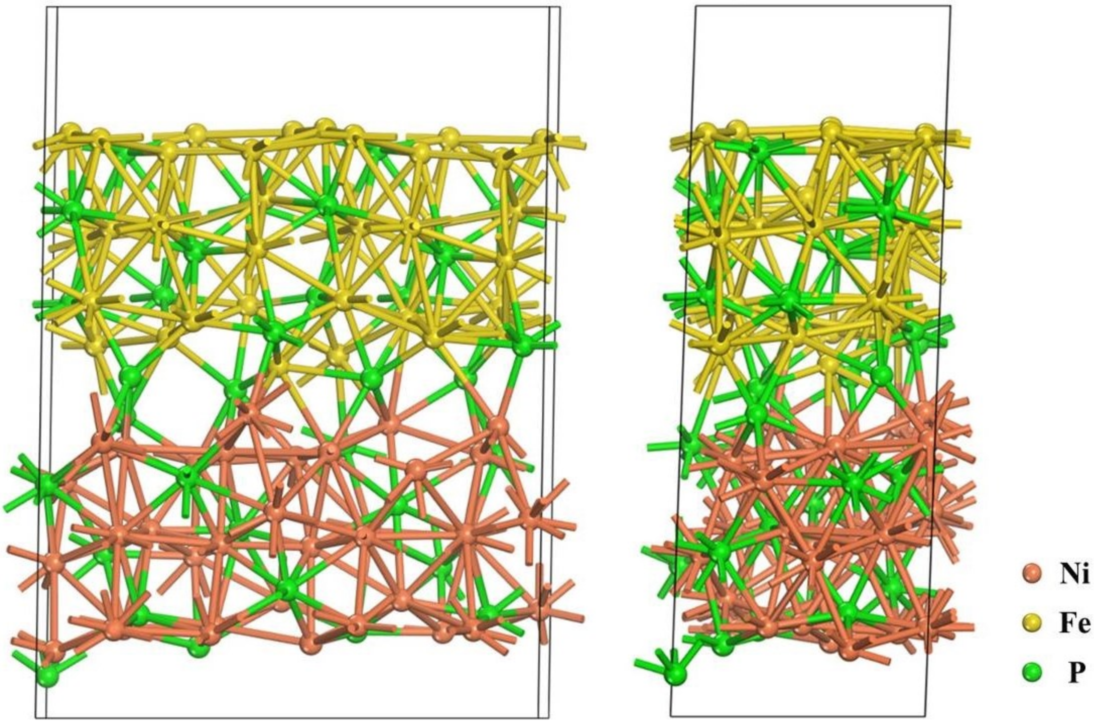

Figure S22. The structure of the heterojunction formed by $Ni_{12}P_5$ and Fe_2P.

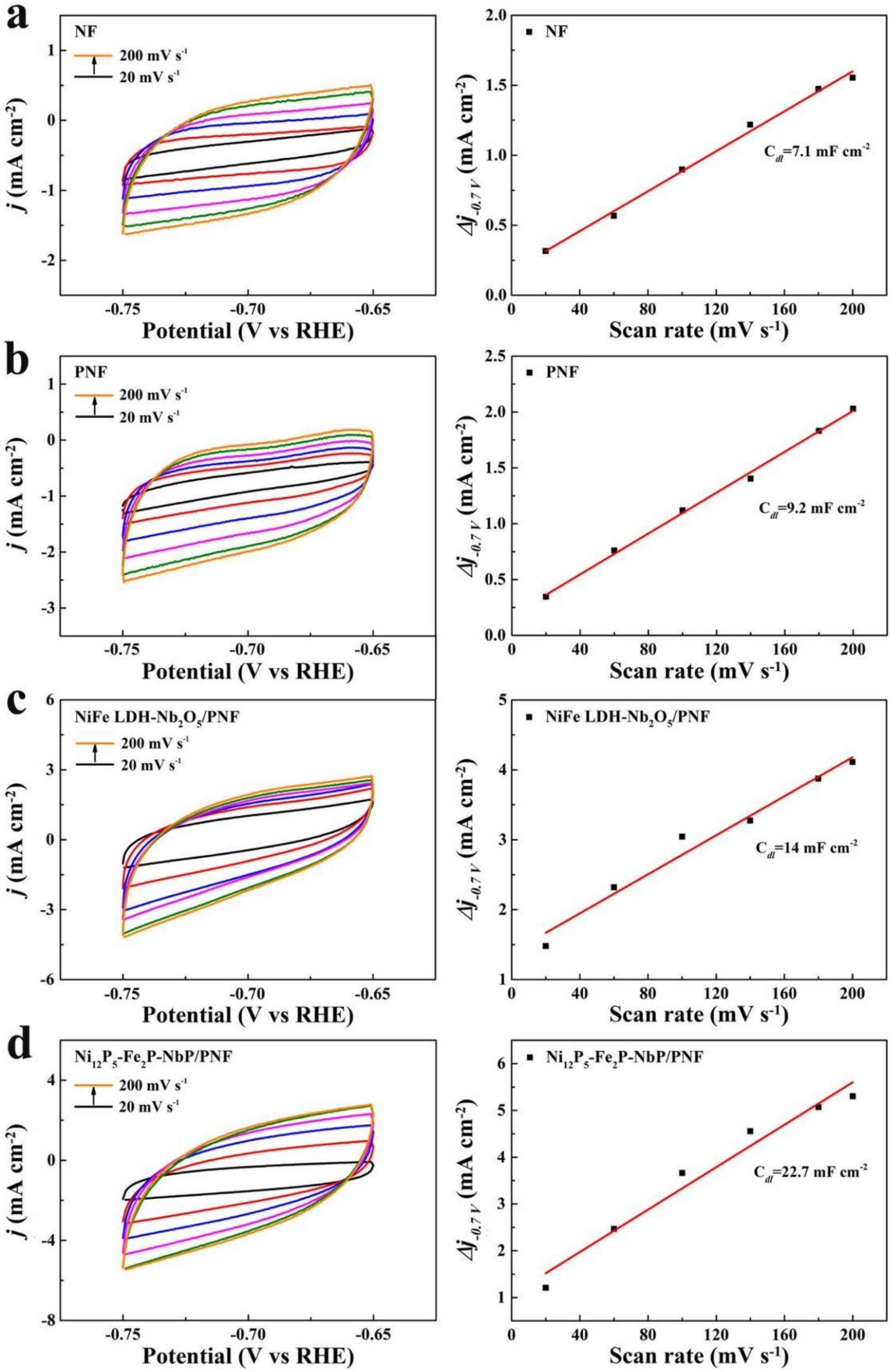

Figure S23. CV curves of electrocatalysts at a scan rate from 20 to 200 mV s^{-1} in 1 M KOH (left) and the calculated C_{dl} (right), (a) NF, (b) PNF, (c) NiFe LDH-Nb_2O_5/PNF and (d) $Ni_{12}P_5$-Fe_2P-NbP/PNF.

3. Supplementary Tables

Table S1. The atomic concentration of different samples.

Element / Atomic %	C1s	O1s	Ni2p	Fe2p	Nb3d	P2p
NiFe LDH-Nb_2O_5/PNF	35.78	40.52	15.34	5.99	2.37	/
$Ni_{12}P_5$-Fe_2P-NbP/PNF	36.89	35.86	8.36	2.75	0.92	15.22
After 100 h HER	37.08	43.30	13.47	2.89	1.61	1.66
After 100 h OER	25.01	50.28	17.68	2.69	1.76	2.58

Table S2. The elemental composition of $Ni_{12}P_5$-Fe_2P-NbP/PNF from ICP-OES.

Element / Atomic %	Ni2p	Fe2p	Nb3d	P2p
$Ni_{12}P_5$-Fe_2P-NbP/PNF	90.75	0.36	1.7	7.18

Table S3. Comparison of electrocatalytic HER activity of various nonprecious catalysts in 1.0 M KOH electrolyte.

Catalysts	η (mV) @ J (mA cm^{-2})	Tafel slope	Stability (h) @ J (mA cm^{-2})	References
$Ni_{12}P_5$-Fe_2P-NbP/PNF	58@10 178@100 244@300 265@400 311@800	52 mV dec^{-1}	100@100 100@300	This Work
$FeCO_3$@IF	151@10 280@100	139 mV dec^{-1}	20@10 45@100	S6
(Ni-Fe)S_x/NiFe$(OH)_y$	124@100	68 mV dec^{-1}	48@120	S7
N-NiVFeP/NFF	79@10 178@50 205@100	78 mV dec^{-1}	100@10 100@100	S8
Am $FePO_4$/NF	123@10 250@100	104 mV dec^{-1}	15@10	S9
$Ni_{0.9}Co_{0.1}O_xH_y$	85@10 180@100	85 mV dec^{-1}	N/A	S10
$CoNiSe_2$@CoNi-LDHs/NF	106@10 228@100	74 mV dec^{-1}	30@50	S11
Nest-like NiCoP/CC	62@10 158@100	68 mV dec^{-1}	15@20	S12
NiFe LDH@NiCoP/NF	120@10 320@100	88 mV dec^{-1}	100@10	S13
Ni_3N-VN/NF	64@10 218@100	37 mV dec^{-1}	20@10	S14

Ni_3Se_4@NiFe LDH/CFC	85@10 220@100	99 mV dec^{-1}	100@10	S15
P-Ni_2P/NF	134@10 250@100	92 mV dec^{-1}	48@100 48@500	S16
Ni_2P/Fe_2P	121@10 300@500	67 mV dec^{-1}	20@100	S17
CoFeP NFs/NPCNT	137@10 198@50	64 mV dec^{-1}	40@10	S18
Meso-Fe-MoS_2/$CoMo_2S_4$	122@10 195@50	90 mV dec^{-1}	20@10	S19

Table S4. TOF for Pt/C/PNF, NiFe LDH-Nb_2O_5/PNF and $Ni_{12}P_5$-Fe_2P-NbP/PNF at the overpotential of 40, 60, 80, 100, 150 and 200 mV in the HER process.

TOF s^{-1}	**Pt/C/PNF**	**NiFe LDH-Nb_2O_5/PNF**	**$Ni_{12}P_5$-Fe_2P-NbP/PNF**
40 mV	7.73×10^{-4}	6.19×10^{-3}	1.37×10^{-2}
60 mV	1.59×10^{-3}	1.07×10^{-2}	2.46×10^{-2}
80 mV	2.92×10^{-3}	1.65×10^{-2}	3.84×10^{-2}
100 mV	4.86×10^{-3}	2.42×10^{-2}	5.85×10^{-2}
150 mV	1.15×10^{-2}	6.46×10^{-2}	1.53×10^{-1}
200 mV	2.37×10^{-2}	1.58×10^{-1}	3.35×10^{-1}

Table S5. The Mass Activity (MA) for Pt/C/PNF, NiFe LDH-Nb_2O_5/PNF and $Ni_{12}P_5$-Fe_2P-NbP/PNF in the HER process.

MA (mA g^{-1})	**Pt/C/PNF**	**NiFe LDH-Nb_2O_5/PNF**	**$Ni_{12}P_5$-Fe_2P-NbP/PNF**
60 mV	7.86×10^2	3.43×10^3	4.18×10^3
80 mV	1.45×10^3	5.25×10^3	6.40×10^3
100 mV	2.40×10^3	7.75×10^3	9.88×10^3
150 mV	5.70×10^3	2.08×10^4	2.59×10^4
200 mV	1.17×10^4	5.09×10^4	5.68×10^4

Table S6. Comparison of evolved H_2 amount occurred on the various nonprecious catalysts electrodes.

Catalysts	Electrolytes	Current Density	H_2 generation amount	References
$Ni_{12}P_5$-Fe_2P-NbP/PNF	1.0 M KOH	10 mA cm^{-2}	1486 μmol h^{-1}	This Work
$FeCO_3$@IF	1.0 M KOH	50 mA cm^{-2}	930 μmol h^{-1}	S6
(Ni-Fe)S_x/NiFe$(OH)_y$	1.0 M KOH	20 mA cm^{-2}	370 μmol h^{-1}	S7
N-NiVFeP/NFF	1.0 M KOH	10 mA cm^{-2}	1610 μmol h^{-1}	S8
Am $FePO_4$/NF	1.0 M KOH	10 mA cm^{-2}	1380 μmol h^{-1}	S9
$CoNiSe_2$@CoNi-LDHs/NF	1.0 M KOH	10 mA cm^{-2}	982 μmol h^{-1}	S11
Ni_3N-VN/NF	1.0 M KOH	10 mA cm^{-2}	470 μmol h^{-1}	S14
CoFeP NFs/NPCNT	1.0 M KOH	10 mA cm^{-2}	175 μmol h^{-1}	S18
Meso-Fe-MoS_2/$CoMo_2S_4$	1.0 M KOH	10 mA cm^{-2}	893 μmol h^{-1}	S19
$NiS_{0.5}Se_{0.5}$	1.0 M KOH	10 mA cm^{-2}	188 μmol h^{-1}	S20
$(FeCoNi)_9S_8$-MoS_2	1.0 M KOH	20 mA cm^{-2}	370 μmol h^{-1}	S21
N-NiCoP/NCF	1.0 M KOH	10 mA cm^{-2}	680 μmol h^{-1}	S22
Cu@NiFe LDH	1.0 M KOH	40 mA cm^{-2}	720 μmol h^{-1}	S23
$Fe_{17.5\%}$-Ni_3S_2/NF	1.0 M KOH	10 mA cm^{-2}	912 μmol h^{-1}	S24

Table S7. Comparison of electrocatalytic OER activity of various nonprecious catalysts in 1.0 M KOH electrolyte.

Catalysts	η (mV) @ J (mA cm^{-2})	Tafel slope	Stability (h) @ J (mA cm^{-2})	References
$Ni_{12}P_5$-Fe_2P-NbP/PNF	260@50 280@100 330@400	59 mV dec^{-1}	100@100 100@300	This Work
$FeCO_3$@IF	273@10 331@100	59 mV dec^{-1}	20@10 30@100	S6
(Ni-Fe)S_x/NiFe$(OH)_y$	199@10 290@100	58 mV dec^{-1}	50@100	S7
N-NiVFeP/NFF	229@10 328@50 386@100	72 mV dec^{-1}	100@10 100@100	S8
Am $FePO_4$/NF	218@10 260@100 270@300	43 mV dec^{-1}	15@10	S9
$Ni_{0.9}Co_{0.1}O_xH_y$	239@10 288@100	46 mV dec^{-1}	N/A	S10
$CoNiSe_2$@CoNi-LDHs/NF	208@10 343@100	39 mV dec^{-1}	48@25	S11
Nest-like NiCoP/CC	242@10 330@100	64 mV dec^{-1}	11@100	S12
NiFe LDH@NiCoP/NF	220@10 360@100	49 mV dec^{-1}	100@10	S13
Ni_2P-VP_2/NF	306@50	49 mV dec^{-1}	20@10	S14

	398@100			
Ni_3Se_4@NiFe LDH/CFC	223@10 250@50 290@100	56 mV dec^{-1}	100@50	S15
Meso-Fe-MoS_2/$CoMo_2S_4$	290@10 333@50 360@100	65 mV dec^{-1}	20@10	S19
$NiTe_2$/$Ni(OH)_2$/CFC	267@10 320@100	75 mV dec^{-1}	30@10	S25
$NiSe_2$/g-C_3N_4	290@40	143 mV dec^{-1}	10@10	S26
Ni-Fe-MOFs NSs	221@10 320@100	56 mV dec^{-1}	20@10	S27

Table S8. TOF for Pt/C/PNF, NiFe LDH-Nb_2O_5/PNF and $Ni_{12}P_5$-Fe_2P-NbP/PNF at the overpotential of 220, 250, 280, 310 and 340 mV in the OER process.

TOF s^{-1}	**RuO_2/PNF**	**NiFe LDH-Nb_2O_5/PNF**	**$Ni_{12}P_5$-Fe_2P-NbP/PNF**
220 mV	1.71×10^{-3}	7.87×10^{-3}	3.96×10^{-2}
250 mV	2.26×10^{-3}	7.9×10^{-3}	4.67×10^{-2}
280 mV	3.17×10^{-3}	9.27×10^{-3}	9.27×10^{-2}
310 mV	5.11×10^{-3}	1.85×10^{-2}	2.34×10^{-1}
340 mV	7.88×10^{-3}	6.24×10^{-2}	4.71×10^{-1}

Table S9. The Mass Activity (MA) for Pt/C/PNF, NiFe LDH-Nb_2O_5/PNF and $Ni_{12}P_5$-Fe_2P-NbP/PNF in the OER process.

MA (mA g^{-1})	**RuO_2/PNF**	**NiFe LDH-Nb_2O_5/PNF**	**$Ni_{12}P_5$-Fe_2P-NbP/PNF**
220 mV	8.13×10^{2}	5.09×10^{2}	1.34×10^{3}
250 mV	1.08×10^{3}	5.44×10^{2}	1.58×10^{3}
280 mV	1.57×10^{3}	6.39×10^{2}	3.15×10^{3}
310 mV	2.43×10^{3}	1.27×10^{3}	7.57×10^{3}
340 mV	3.75×10^{3}	4.31×10^{3}	1.53×10^{4}

Table S10. Comparison of the evolved O_2 amount generated on the various nonprecious catalysts electrodes.

Catalysts	Electrolytes	Current Density	O_2 generation amount	References
$Ni_{12}P_5$-Fe_2P-NbP/PNF	1.0 M KOH	10 mA cm^{-2}	708 μmol h^{-1}	This Work
$FeCO_3$@IF	1.0 M KOH	50 mA cm^{-2}	460 μmol h^{-1}	S6
(Ni-Fe)S_x/NiFe$(OH)_y$	1.0 M KOH	20 mA cm^{-2}	180 μmol h^{-1}	S7
N-NiVFeP/NFF	1.0 M KOH	10 mA cm^{-2}	810 μmol h^{-1}	S8
Am $FePO_4$/NF	1.0 M KOH	10 mA cm^{-2}	629 μmol h^{-1}	S9
$CoNiSe_2$@CoNi-LDHs/NF	1.0 M KOH	10 mA cm^{-2}	446 μmol h^{-1}	S11
Ni_2P-VP_2/NF	1.0 M KOH	10 mA cm^{-2}	230 μmol h^{-1}	S14
CoFeP NFs/NPCNT	1.0 M KOH	10 mA cm^{-2}	88 μmol h^{-1}	S18
Meso-Fe-MoS_2/$CoMo_2S_4$	1.0 M KOH	10 mA cm^{-2}	455 μmol h^{-1}	S19
$NiS_{0.5}Se_{0.5}$	1.0 M KOH	10 mA cm^{-2}	89 μmol h^{-1}	S20
$(FeCoNi)_9S_8$-MoS_2	1.0 M KOH	20 mA cm^{-2}	180 μmol h^{-1}	S21
N-NiCoP/NCF	1.0 M KOH	10 mA cm^{-2}	400 μmol h^{-1}	S22
Cu@NiFe LDH	1.0 M KOH	40 mA cm^{-2}	340 μmol h^{-1}	S23
$Fe_{17.5\%}$-Ni_3S_2/NF	1.0 M KOH	10 mA cm^{-2}	463 μmol h^{-1}	S24

Table S11. Comparison of the full water-splitting performances of $Ni_{12}P_5$-Fe_2P-NbP/PNF with other state-of-the-art electrocatalysts in 1.0 M KOH.

Catalysts	**Cell voltages (V) @ *J* (mA cm^{-2})**	**References**
$Ni_{12}P_5$-Fe_2P-NbP/PNF	1.51@10 1.58@50 1.65@100 1.74@200	This Work
$FeCO_3$@IF	1.69@10 2.36@300 2.51@400	S6
(Ni-Fe)S_x/NiFe$(OH)_y$	1.46@10 1.73@100	S7
N-NiVFeP/NFF	1.52@10 1.68@100	S8
Am $FePO_4$/NF	1.54@10 1.72@100	S9
$Ni_{0.9}Co_{0.1}O_xH_y$	1.58@10 1.72@50	S10
$CoNiSe_2$@CoNi-LDHs/NF	1.44@10 1.65@50 1.69@100	S11
Nest-like NiCoP/CC	1.52@10 1.77@100	S12
NiFe LDH@NiCoP/NF	1.57@10 1.91@100	S13

Ni_3N-VN/NF‖Ni_2P-VP_2/NF	1.51@10 1.74@50	S14
Ni_3Se_4@NiFe LDH/CFC	1.54@10 1.76@100	S15
Meso-Fe-MoS_2/$CoMo_2S_4$	1.62@10 1.78@50	S19
$NiS_{0.5}Se_{0.5}$	1.55@10 1.74@100	S20
Cu@NiFe LDH	1.54@10 1.69@100	S23
$Fe_{17.5\%}$-Ni_3S_2/NF	1.54@10 1.60@20 1.70@100	S24

References

[S1] Q. Zhang, W. Chen, G. Chen, J. Huang, C. Song, S. Chu, R. Zhang, G. Wang, C. Li, K.K. Ostrikov, Bi-metallic nitroxide nanodot-decorated tri-metallic sulphide nanosheets by on-electrode plasma-hydrothermal sprouting for overall water splitting. Appl. Catal. B: Environ. 2020, **261**, 118254.

[S2] L. Meng, J. He, W. Tian, M. Wang, R. Long, L. Li, Ni/Fe Codoped In_2S_3 Nanosheet Arrays Boost Photo-Electrochemical Performance of Planar Si Photocathodes. Adv. Energy Mater. 2019, **9**(38), 1902135.

[S3] S. Qu, W. Chen, J. Yu, G. Chen, R. Zhang, S. Chu, J. Huang, X. Wang, C. Li, K. Ostrikov, Cross-linked trimetallic nanopetals for electrocatalytic water splitting. J. Power Sources 2018, **390**, 224-233.

[S4] R. Jin, J. Huang, G. Chen, W. Chen, B. Ouyang, D. Chen, E. Kan, H. Zhu, C. Li, D. Yang, K. Ostrikov, Water-sprouted, plasma-enhanced Ni-Co phospho-nitride nanosheets boost electrocatalytic hydrogen and oxygen evolution. Chem. Engineering J. 2020, **402**, 126257.

[S5] J. Huang, S. Wen, G. Chen, W. Chen, G. Wang, H. Fan, D. Chen, C. Song, M. Li, X. Wang, L. Li, M. Tao, B. Li, X. Wang, K. Ostrikov, Multiphase Ni-Fe-selenide nanosheets for highly-efficient and ultra-stable water electrolysis. Appl. Catal. B: Environ. 2020, **277**, 119220.

[S6] T. Gao, C. Zhou, X. Chen, Z. Huang, H. Yuan, D. Xiao, Surface in situ self-reconstructing hierarchical structures derived from ferrous carbonate as efficient bifunctional iron-based catalysts for oxygen and hydrogen evolution reactions. Journal of Materials Chemistry A 2020, **8**, 18367-18375.

[S7] Q. Che, Q. Li, Y. Tan, X. Chen, X. Xu, Y. Chen, One-step controllable synthesis of amorphous $(Ni\text{-}Fe)S_x/NiFe(OH)_y$ hollow microtube/sphere films as superior bifunctional electrocatalysts for quasi-industrial water splitting at large-current-density. Applied Catalysis B: Environmental 2019, **246**, 337-348.

[S8] H. Fan, W. Chen, G. Chen, J. Huang, C. Song, Y. Du, C. Li, K. Ostrikov, Plasma-heteroatom-doped Ni-V-Fe trimetallic phospho-nitride as high-performance bifunctional electrocatalyst. Applied Catalysis B: Environmental 2020, **268**, 118440.

[S9] L. Yang, Z. Guo, J. Huang, Y. Xi, R. Gao, G. Su, W. Wang, L. Cao, B. Dong, Vertical Growth of 2D Amorphous $FePO_4$ Nanosheet on Ni Foam: Outer and Inner Structural Design for Superior Water Splitting. Advanced Materials 2017, **29**, 1704574.

[S10] Q. Zhao, J. Yang, M. Liu, R. Wang, G. Zhang, H. Wang, H. Tang, C. Liu, Z. Mei, H. Chen, F. Pan, Tuning Electronic Push/Pull of Ni-Based Hydroxides To Enhance Hydrogen and Oxygen Evolution Reactions for Water Splitting. ACS Catalysis 2018, **8**, 5621-5629.

[S11] Y. Yang, W. Zhang, Y. Xiao, Z. Shi, X. Cao, Y. Tang, Q. Gao, $CoNiSe_2$ heteronanorods decorated with layered-double-hydroxides for efficient hydrogen evolution. Applied Catalysis B: Environmental 2019, **242**, 132-139.

[S12] C. Du, L. Yang, F. Yang, G. Cheng, W. Luo, Nest-like NiCoP for Highly Efficient Overall Water Splitting. ACS Catalysis 2017, **7**, 4131-4137.

[S13] H. Zhang, X. Li, A. Hähnel, V. Naumann, C. Lin, S. Azimi, S.L. Schweizer, A.W. Maijenburg, R.B. Wehrspohn, Bifunctional Heterostructure Assembly of NiFe LDH Nanosheets on NiCoP Nanowires for Highly Efficient and Stable Overall Water Splitting. Advanced Functional Materials 2018, **28**, 1706847.

[S14] H. Yan, Y. Xie, A. Wu, Z. Cai, L. Wang, C. Tian, X. Zhang, H. Fu, Anion-Modulated HER and OER Activities of 3D Ni-V-Based Interstitial Compound Heterojunctions for High-Efficiency and Stable Overall Water Splitting. Advanced Materials 2019, **31**, 1901174.

[S15] T. Zhang, L. Hang, Y. Sun, D. Men, X. Li, L. Wen, X. Lyu, Y. Li, Hierarchical hetero-Ni_3Se_4@NiFe LDH micro/nanosheets as efficient bifunctional electrocatalysts with superior stability for overall water splitting. Nanoscale Horizons 2019, **4**, 1132-1138.

[S16] X. Jin, J. Li, Y. Cui, X. Liu, K. Wang, Y. Zhou, W. Yang, X. Zhang, C. Zhang, X. Jiang, B. Liu, In-situ synthesis of porous Ni_2P nanosheets for efficient and stable hydrogen evolution reaction. International Journal of Hydrogen Energy 2019, **44**, 5739-5747.

[S17] Y. Ge, P. Dong, S.R. Craig, P.M. Ajayan, M. Ye, J. Shen, Transforming Nickel Hydroxide into 3D Prussian Blue Analogue Array to Obtain Ni_2P/Fe_2P for Efficient Hydrogen Evolution Reaction. Advanced Energy Materials 2018, **8**, 1800484.

[S18] W. Li, Y. Chen, B. Yu, Y. Hu, X. Wang, D. Yang, 3D hollow Co-Fe-P nanoframes immobilized on N,P-doped CNT as an efficient electrocatalyst for overall water splitting. Nanoscale 2019, **11**, 17031-17040.

[S19] Y. Guo, J. Tang, J. Henzie, B. Jiang, W. Xia, T. Chen, Y. Bando, Y.M. Kang, M.S.A. Hossain, Y. Sugahara, Y. Yamauchi, Mesoporous Iron-doped $MoS_2/CoMo_2S_4$ Heterostructures through Organic-Metal Cooperative Interactions on Spherical Micelles for Electrochemical Water Splitting. ACS Nano 2020, **14**, 4141-4152.

[S20] Y. Wang, X. Li, M. Zhang, Y. Zhou, D. Rao, C. Zhong, J. Zhang, X. Han, W. Hu, Y. Zhang, K. Zaghib, Y. Wang, Y. Deng, Lattice-Strain Engineering of Homogeneous $NiS_{0.5}Se_{0.5}$ Core-Shell Nanostructure as a Highly Efficient and Robust Electrocatalyst for Overall Water Splitting. Advanced Materials 2020, **32**, 2000231.

[S21] H. Li, S. Chen, Y. Zhang, Q. Zhang, X. Jia, Q. Zhang, L. Gu, X. Sun, L. Song, X. Wang, Systematic design of superaerophobic nanotube-array electrode comprised of transition-metal sulfides for overall water splitting. Nature Communications 2018, **9**, 2452.

[S22] R. Zhang, J. Huang, G. Chen, W. Chen, C. Song, C. Li, K. Ostrikov, In situ engineering bi-metallic phospho-nitride bi-functional electrocatalysts for overall water splitting. Applied Catalysis B: Environmental 2019, **254**, 414-423.

[S23] L. Yu, H. Zhou, J. Sun, F. Qin, F. Yu, J. Bao, Y. Yu, S. Chen, Z. Ren, Cu nanowires shelled with NiFe layered double hydroxide nanosheets as bifunctional electrocatalysts for overall water splitting. Energy & Environmental Science 2017, **10**, 1820-1827.

[S24] G. Zhang, Y.S. Feng, W.T. Lu, D. He, C.Y. Wang, Y.K. Li, X.Y. Wang, F.F. Cao, Enhanced Catalysis of Electrochemical Overall Water Splitting in Alkaline Media by Fe Doping in Ni_3S_2 Nanosheet Arrays. ACS Catalysis 2018, **8**, 5431-5441.

[S25] B. Xu, X. Yang, X. Liu, W. Song, Y. Sun, Q. Liu, H. Yang, C. Li, Lattice distortion in hybrid $NiTe_2/Ni(OH)_2$ nanosheets as efficient synergistic electrocatalyst for water and urea oxidation. Journal of Power Sources 2020, **449**, 227585.

[S26] S. Wang, P. He, L. Jia, M. He, T. Zhang, F. Dong, M. Liu, H. Liu, Y. Zhang, C. Li, J. Gao, L. Bian, Nanocoral-like composite of nickel selenide nanoparticles anchored on two-dimensional multi-layered graphitic carbon nitride: A highly efficient electrocatalyst for oxygen evolution reaction. Applied Catalysis B: Environmental 2019, **243**, 463-469.

[S27] F. Li, P. Wang, X. Huang, D.J. Young, H. Wang, P. Braunstein, J. Lang, Large-Scalable, Bottom-Up Synthesis of Binary Metal-Organic Framework Nanosheets for Efficient Water Oxidation. Angewandte Chemie International Edition 2019, **58**, 7051-7056.